

Subcycle quantum electrodynamics

C. Riek¹, P. Sulzer¹, M. Seeger¹, A. S. Moskalenko¹, G. Burkard¹, D. V. Seletskiy¹ & A. Leitenstorfer¹

Squeezed states^{1–4} of electromagnetic radiation have quantum fluctuations below those of the vacuum field. They offer a unique resource for quantum information systems⁵ and precision metrology⁶, including gravitational wave detectors, which require unprecedented sensitivity⁷. Since the first experiments on this non-classical form of light^{8,9}, quantum analysis has been based on homodyning techniques and photon correlation measurements^{10,11}. These methods currently function in the visible to near-infrared and microwave¹² spectral ranges. They require a well-defined carrier frequency, and photons contained in a quantum state need to be absorbed or amplified. Quantum non-demolition experiments^{13,14} may be performed to avoid the influence of a measurement in one quadrature, but this procedure comes at the expense of increased uncertainty in another quadrature. Here we generate mid-infrared time-locked patterns of squeezed vacuum noise. After propagation through free space, the quantum fluctuations of the electric field are studied in the time domain using electro-optic sampling with few-femtosecond laser pulses^{15,16}. We directly compare the local noise amplitude to that of bare (that is, unperturbed) vacuum. Our nonlinear approach operates off resonance and, unlike homodyning or photon correlation techniques, without absorption or amplification of the field that is investigated. We find subcycle intervals with noise levels that are substantially less than the amplitude of the vacuum field. As a consequence, there are enhanced fluctuations in adjacent time intervals, owing to Heisenberg's uncertainty principle, which indicate generation of highly correlated quantum radiation. Together with efforts in the far infrared^{17,18}, this work enables the study of elementary quantum dynamics of light and matter in an energy range at the boundary between vacuum and thermal background conditions.

In quantum electrodynamics, coherent states represent the closest counterparts to a classical electromagnetic wave. The quantum noise amplitudes of their electric and magnetic fields coincide precisely with those of the vacuum state¹⁹. Recently, the bare vacuum fluctuations of the mid-infrared (MIR) electric field were directly detected using highly sensitive electro-optic sampling based on ultrashort laser pulses^{15,16}. One key aspect of this technique is that it operates in the time domain. Therefore, it should provide a resolution that is substantially below the duration of an oscillation period of any quantum field under study. It is tempting to consider an experiment that synchronously couples a non-classical state of light into the space-time volume that is probed, thus providing a quantum noise amplitude that deviates from pure vacuum fluctuations. An especially striking manifestation of quantum physics would be to demonstrate a spatial and temporal localization of less noise than that of the quantum vacuum. In conventional homodyning studies, the carrier wave of a local oscillator needs to be phase-locked to a quantum state^{11,16}. In contrast, here we prepare a squeezed electromagnetic transient with a noise pattern that is synchronized with the intensity envelope of an ultrashort probe pulse. This tightly focused few-femtosecond optical wave packet then defines a subcycle space-time segment in which the quantum statistics of a MIR non-classical signal is sampled.

Our scheme to implement such an experiment is sketched in Fig. 1a. We send an intense near-infrared (NIR) pump pulse (red/yellow

envelope) with a duration of 12 fs and centre frequency of 200 THz into a thin generation crystal (GX). In a first step, a carrier-envelope phase-locked electric field transient²⁰ is generated by optical rectification (red line). Once built up, this transient starts to locally phase shift the co-propagating MIR vacuum fluctuations (green shaded band). This second step is achieved by means of the electro-optic effect in the GX, which establishes a change in refractive index $\Delta n(t)$ proportional to the MIR electric field amplitude $E_{\text{MIR}}(t)$. In a simplified picture, the resulting local anomalies in the speed of light might induce depletion of vacuum amplitude in certain space-time regions (blue shaded sections in Fig. 1a), piling it up in others (shaded in red). A high efficiency for this two-step mechanism to squeeze the MIR vacuum is ensured by the large second-order nonlinearity of the 16- μm -thick exfoliated piece of GaSe we use as the GX²⁰. Tight focusing of the pump to a paraxial spot radius w_{pump} of 3.6 μm also defines the transverse spatial mode for the non-classical electric field pattern. After the MIR field exits the GX, it is collimated and the residual pump is removed by a 70- μm -thick GaSb filter inserted at Brewster's angle. A mode-matched 5.8-fs probe pulse (blue envelope in Fig. 1a) is then superimposed onto the MIR field and focused to $w_{\text{probe}} = 3.6 \mu\text{m}$ in a AgGaS₂ detector crystal (DX) with a thickness of 24 μm (ref. 15). The probe pulse samples the electric field in the co-propagating space-time volume via the electro-optic effect^{15,20} and as a function of time delay t_D . We gain two different types of information: first, the coherent¹⁹ electric field amplitude $E_{\text{MIR}}(t_D)$ of the squeezing MIR transient is recorded in the conventional way²⁰; and second, the quantum distribution of the MIR electric field is accessed via statistical readout¹⁵. Our technique allows us to directly reference the local noise level ΔE_{rms} in a squeezed transient (blue and red distributions in Fig. 1b) to the fluctuations ΔE_{vac} obtained under bare vacuum input (green distribution in Fig. 1b; see Methods for details). Relative differential noise (RDN) patterns mirroring ΔE_{rms} are then recorded as a function of delay time t_D (see Fig. 1c). Only 4% of the total fluctuation amplitude in our set-up results from a bare MIR vacuum input; the rest is due to the noise-equivalent field of the detector ΔE_{SN} caused by the quantized flux of NIR probe photons¹⁵ (see Methods for details). Therefore, a RDN of -0.04 would correspond to a complete removal of the vacuum fluctuations in the space-time segment sampled in the DX.

The coherent field transients $E_{\text{MIR}}(t_D)$ generated by optical rectification of a NIR 12-fs pump with a pulse energy of 3.5 nJ are depicted in Fig. 2a. Two waveforms with precisely inverted amplitudes result from rotation of the pump polarization by 90° around the optical axis (black and grey lines). The broadband amplitude spectra (inset) have an average frequency of 44 THz, corresponding to a free-space wavelength of 6.8 μm and photon energy of 180 meV. Figure 2b shows the RDN amplitudes recorded simultaneously. Dark (light) blue areas denote delay times with negative values induced by the black (grey) transient in Fig. 2a, indicating a clear squeezing of the local electric field fluctuations ΔE_{rms} below the level of the bare quantum vacuum. Time segments carrying excess noise with respect to the vacuum ground state are filled in red. Salient features in the noise patterns in Fig. 2b are evident. First, there is a clear asymmetry, with positive excess noise surpassing the absolute values of vacuum squeezing, especially in the region close to the centre of the transients where the amplitudes

¹Department of Physics and Center for Applied Photonics, University of Konstanz, D-78457 Konstanz, Germany.

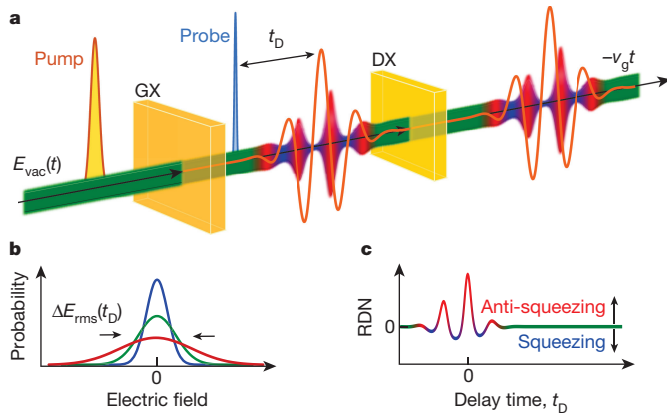


Figure 1 | Scheme for time-locked generation and detection of quantum transients by electro-optic sampling. **a**, A 12-fs near-infrared (NIR) pump pulse (red/yellow envelope) and mid-infrared (MIR) vacuum fluctuations (green band; with amplitude ΔE_{vac}) co-propagate into a generation crystal (GX) with second-order nonlinearity. A coherent MIR transient results (red line), which squeezes the quantum vacuum (red and blue shading). A 6-fs probe pulse (blue envelope) is superimposed to sample the electric field amplitude as a function of delay time t_D in an electro-optic detector crystal (DX). Propagation occurs along a spatial coordinate proportional to the product of the negative group velocity $-v_g$ and time t . **b**, Sketch of the probability distributions of the electric field at t_D , illustrated at negligible coherent amplitude for bare vacuum (green), squeezing (blue) or anti-squeezing (red). The arrows indicate that the local noise level $\Delta E_{\text{rms}}(t_D)$ is defined as the root-mean-square (r.m.s.) standard deviation of the probability distribution at delay time t_D . **c**, Illustration of a trace of the relative differential noise (RDN $\approx [\Delta E_{\text{rms}}(t_D) - \Delta E_{\text{vac}}]\Delta E_{\text{vac}} / \Delta E_{\text{SN}}^2$, where ΔE_{SN} is the noise-equivalent field of the detector) of the quantum field as sampled versus delay time t_D . The green segments signify time intervals with quantum noise at the level of bare vacuum fluctuations, at which RDN = 0. Regions of positive excess noise (anti-squeezing; red) and negative excess noise (squeezing; blue) are indicated by the arrows pointing upwards and downwards, respectively.

are greatest. Second, the noise maxima in Fig. 2b coincide with the maximally positive slopes of the coherent field amplitudes in Fig. 2a, while optimum squeezing of $\Delta E_{\text{rms}}(t_D)$ is obtained close to the positions with a maximal decrease in $E_{\text{MIR}}(t_D)$ with time (see vertical dashed lines). Finally, owing to this inherent polar asymmetry in ΔE_{rms} , the shift in carrier-envelope phase between the black and grey transients in Fig. 2a results in distinctly different quantum noise patterns that are not mirror images of each other.

We now investigate the physical origin of these findings. We first vary the pulse energy in the NIR pump, which is proportional to the electric field amplitude E_{MIR} , and record the resulting RDN amplitudes (Fig. 3). At low pump energies of 0.8 nJ and 1.5 nJ, the noise patterns are still fairly symmetric with respect to positive and negative extrema. The asymmetry towards positive excess noise appears clearly at 2.5 nJ and becomes distinct at 3.5 nJ. The origin of these observations is qualitatively understood in terms of the following expression for $\Delta E_{\text{rms}}(t)$ at the exit surface of a GX (see Methods for details):

$$\Delta E_{\text{rms}}(t) = e^{f(t)} \Delta E_{\text{vac}} \quad (1)$$

where

$$f(t) = \frac{dl}{nc} \frac{\partial E_{\text{MIR}}(t)}{\partial t} \quad (2)$$

denotes the squeezing factor in the time domain. We adopt plane waves and negligible pump depletion in a medium with a second-order nonlinear coefficient d and thickness l . The bare vacuum amplitude ΔE_{vac} is assumed as input, which is adequate for the quantum

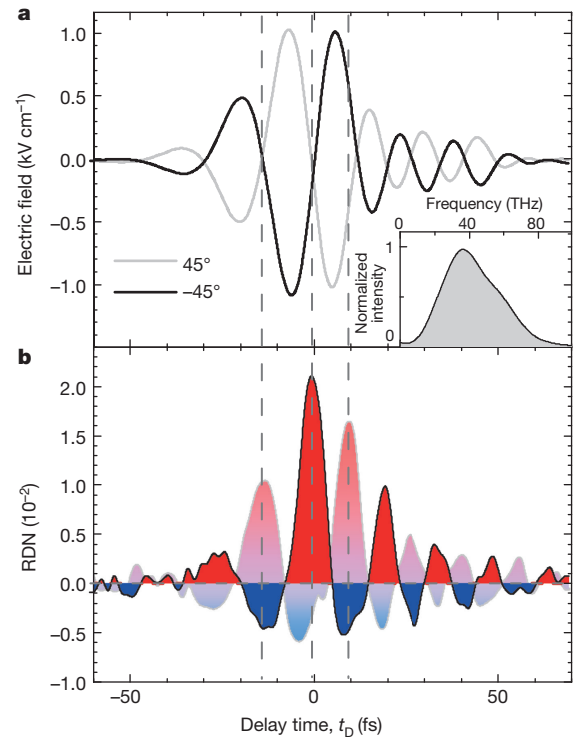


Figure 2 | RDN patterns and dependence on carrier-envelope phase of generating coherent field. **a**, Complementary electric field amplitude of coherent MIR transients sampled in the electro-optic detector, obtained with two different settings of NIR pump polarization (grey, 45°; black, -45°) on the GaSe emitter crystal GX. The inset shows the amplitude spectrum. **b**, RDN traces, recorded at the same time as the coherent signals in **a**. Sections with less noise as compared to the bare vacuum are depicted in blue; excess noise is shown in red. The strongly (lightly) coloured squeezing pattern with black (grey) envelope corresponds to the black (grey) transient in **a**. The vertical dashed lines highlight the phase relationship between **a** and **b**.

properties of the coherent pump. c denotes the speed of light in vacuum and the assumption of a constant refractive index n is well justified because of the minor dispersion of GaSe in the MIR. It is evident from equations (1) and (2) that the extrema in $\Delta E_{\text{rms}}(t)$ are expected at the positions of maximum slope of $E_{\text{MIR}}(t)$, as confirmed experimentally in Fig. 2. With increasing $E_{\text{MIR}}(t)$, a nonlinear relationship between squeezing and excess noise, referenced to ΔE_{vac} , results because of the exponential character of equation (1). This relationship tentatively explains the build-up of the asymmetry in Fig. 3. We now select two points in time, t_{max} and t_{min} , at which the slope of $E_{\text{MIR}}(t)$ differs only by sign: $f(t_{\text{max}}) = |f(t_{\text{max}})| = -f(t_{\text{min}})$. With equations (1) and (2) and the quantitative expression for the vacuum amplitude¹⁶ we obtain

$$\Delta E_{\text{rms}}(t_{\text{min}}) \Delta E_{\text{rms}}(t_{\text{max}}) = (\Delta E_{\text{vac}})^2 = \frac{\hbar}{\varepsilon_0 \Delta x \Delta y \Delta z \Delta t} \quad (3)$$

where a four-dimensional space-time segment is defined by the transverse modal cross-section $\Delta x \Delta y = w_{\text{probe}}^2 \pi$ and the effective spatio-temporal length $\Delta z \Delta t$ that is set by the intensity envelope of the probe¹⁵, \hbar is the reduced Planck constant and ε_0 is the permittivity of free space. To experimentally verify equation (3), two delay times with extremal time derivatives of $E_{\text{MIR}}(t)$ are sampled. We plot the measured values for RDN(t_{max}) and RDN(t_{min}) versus NIR pump pulse energy (red and blue circles in Fig. 4, respectively). The green curves represent a least-squares fit to the data based solely on equation (3). Saturation behaviour is found for squeezing and a superlinear increase is found for anti-squeezing, demonstrating good agreement between experiment and theory. The free parameter that determines the asymmetry between

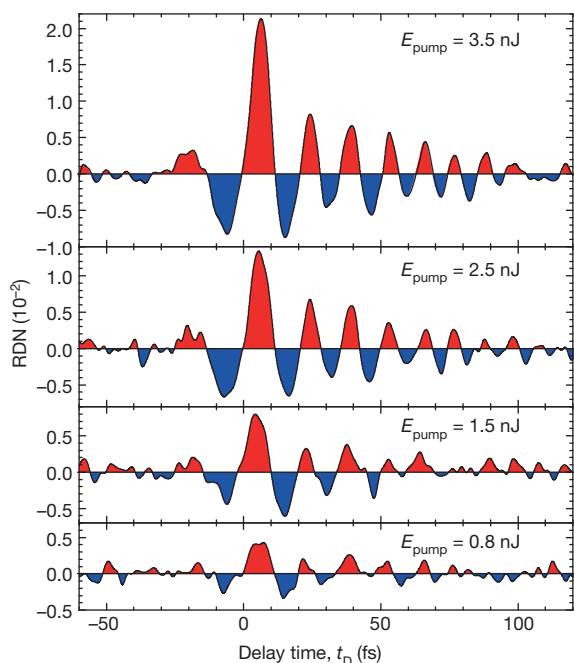


Figure 3 | Development of RDN patterns for different NIR pump pulse energies. Blue-filled sections indicate squeezing with respect to the bare vacuum electric field amplitude; red areas denote anti-squeezing. An asymmetry between negative and positive values builds up with increasing NIR pump pulse energy E_{pump} . The GaSe emitter crystal has a thickness of $l = 16 \mu\text{m}$, and the angle between the beam direction and the optical axis is $\theta = 0^\circ$; for the AgGaS₂ DX, $l = 24 \mu\text{m}$ and $\theta = 48^\circ$.

the green curves in Fig. 4 can be exploited to calibrate the amount of squeezing that is achieved in the experiment (right axis in Fig. 4). A value of $1 - \exp[-f(t_{\text{min}})]$ of close to 50% is obtained at a pump energy of 3.5 nJ, which corresponds to a decrease in RDN amplitude in the electro-optic signal by approximately 10^{-2} (left axis in Fig. 4). The asymmetry originates from the maximum squeezing of the MIR quantum field that is achieved inside the GX. Spurious reflections at the uncoated surfaces of the GX and DX as well as imperfect segment matching to the spatio-temporal probe wave packet contaminate the non-classical state with bare vacuum noise. Therefore, the 50% of local squeezing inside the GX inferred by the analysis and a resulting RDN of -0.01 (see Fig. 4) are compatible with the maximal noise change of -0.04 that would result under complete suppression of MIR vacuum fluctuations in the DX.

We now consider the physical character and origin of the squeezed wave packets that we sample. From Fig. 2 and the discussion of equations (1) and (2), it is evident that the quantum noise patterns $\Delta E_{\text{rms}}(t_D)$ exhibit approximately the same temporal periodicity as the field transients $E_{\text{MIR}}(t_D)$. Consequently, the total quantum state corresponds to neither amplitude nor phase squeezing of the coherent transients $E_{\text{MIR}}(t_D)$. To detect non-classical behaviour with a conventional method such as balanced homodyning, a coherent field centred at half the carrier frequency of $E_{\text{MIR}}(t_D)$ (that is, around 22 THz) would have to be used as a local oscillator. This situation is analogous to established squeezing experiments based on a second-order nonlinearity and spontaneous parametric fluorescence⁹. Our noise patterns therefore correspond to an ultrabroadband generation of correlated photon pairs^{21,22} by $E_{\text{MIR}}(t_D)$, with total energies distributed symmetrically around the carrier frequency of 44 THz (ref. 16). Owing to the quadratic dependence of the intensity on electric field amplitude, the symmetric deviations from the vacuum level detected under low pump conditions in Figs 3 and 4 already indicate the generation of finite energy in the form of highly correlated photon pairs. This is in agreement with the fact that there is only one unique ground state¹⁹.

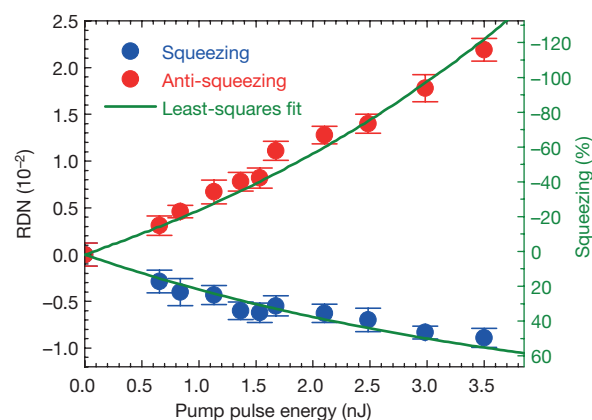


Figure 4 | Build-up of asymmetry between squeezing and anti-squeezing as a consequence of the uncertainty principle. Extremal values of RDN at a maximally squeezed temporal position (blue circles) and for adjacent excess fluctuations (red circles) are plotted versus NIR pump pulse energy. The green line represents a least-squares fit to the data based on equation (3), yielding the relative squeezing values (right axis), which refer to the quantum state inside the GX. Error bars refer to the standard deviation of the RDN signal in each individual measurement, as taken over an interval of negative time delays for which there is no deviation from the vacuum level.

The asymmetry that shows up at higher pump fluences, in accord with the exponent in equation (1) (defined in equation (2)), marks the transition into a regime with higher-order correlations. On sub-cycle scales, these photons remain indistinguishable. Their correlated behaviour with respect to losses induced by diffraction and the partially reflecting facets of the GX and DX²³ results in conservation of the ratio between squeezing and excess noise, despite statistical admixture of uncorrelated vacuum signals. Traditionally, squeezing has been considered in the frequency domain, and is attributed to amplification and de-amplification of specific field quadratures²⁴. But the electro-optic effect motivated in the introduction links the $\partial E_{\text{MIR}}/\partial t$ term in equation (2) to a modulation of the refractive index $\partial n/\partial t$. Therefore, redistribution of vacuum fluctuations following local advancement and slowdown of the speed of light²⁵ represents an attractive alternative with which to illustrate generation of non-classical radiation in our subcycle time-resolved situation. The time-domain manifestation of Heisenberg's uncertainty principle in equation (3) leads to an imbalance between the excess noise related to acceleration of the co-propagating reference frame and squeezing of the quantum amplitude that originates from local deceleration (see Methods).

In conclusion, a time-domain perspective on quantum electrodynamics works with subcycle resolution and direct referencing of electric field fluctuations to the quantum vacuum. The high peak intensities provided by few-femtosecond laser pulses of minute energy content enable a compact quantum technology based on broadband nonlinearities without immediate need for enhancement cavities, waveguides or cryogenic cooling. Many fundamental questions arise concerning a generalized understanding of quadratures being linked to local accelerations of the moving reference frame and regarding the benefits and limitations of the inherently non-destructive character of the technique. Future extensions could aim to achieve, for example, a full quantum tomography²⁶ on subcycle scales. Filling the gap created by a lack of quantum approaches in the MIR or multi-terahertz range provides interesting perspectives: access to new quantum states produced by subcycle perturbation of ultrastrongly coupled light-matter systems²⁷ might be one application; quantum spectroscopy²⁸ and manipulation of collective degrees of freedom in condensed matter are also inherent to this regime.

Online Content Methods, along with any additional Extended Data display items and Source Data, are available in the online version of the paper; references unique to these sections appear only in the online paper.

Received 13 July; accepted 24 November 2016.

1. Stoler, D. Equivalence classes of minimum uncertainty packets. *Phys. Rev. D* **1**, 3217–3219 (1970).
2. Hollenhorst, J. N. Quantum limits on resonant-mass gravitational-radiation detectors. *Phys. Rev. D* **19**, 1669–1679 (1979).
3. Walls, D. F. Squeezed states of light. *Nature* **306**, 141–146 (1983).
4. Loudon, R. & Knight, P. L. Squeezed light. *J. Mod. Opt.* **34**, 709–759 (1987).
5. Braunstein, S. L. & van Loock, P. Quantum information with continuous variables. *Rev. Mod. Phys.* **77**, 513–577 (2005).
6. Caves, C. M. Quantum-mechanical noise in an interferometer. *Phys. Rev. D* **23**, 1693–1708 (1981).
7. The LIGO Scientific Collaboration. Enhanced sensitivity of the LIGO gravitational wave detector by using squeezed states of light. *Nat. Photon.* **7**, 613–619 (2013).
8. Slusher, R. E., Hollberg, L. W., Yurke, B., Mertz, J. C. & Valley, J. F. Observation of squeezed states generated by four-wave mixing in an optical cavity. *Phys. Rev. Lett.* **55**, 2409–2412 (1985).
9. Wu, L.-A., Kimble, H. J., Hall, J. L. & Wu, H. Generation of squeezed states by parametric down conversion. *Phys. Rev. Lett.* **57**, 2520–2523 (1986).
10. Altepeter, J. B., James, D. F. V. & Kwiat, P. G. in *Quantum State Estimation* (eds Paris, M. G. A. & Reháček, J.) 113–145 (*Lecture Notes in Physics* Vol. 649, Springer, 2004).
11. Lvovsky, A. I. & Raymer, M. G. Continuous-variable optical quantum-state tomography. *Rev. Mod. Phys.* **81**, 299–332 (2009).
12. Devoret, M. H. & Schoelkopf, R. J. Superconducting circuits for quantum information: an outlook. *Science* **339**, 1169–1174 (2013).
13. Levenson, M. D., Shelby, R. M., Reid, M. & Walls, D. F. Quantum nondemolition detection of optical quadrature amplitudes. *Phys. Rev. Lett.* **57**, 2473–2476 (1986).
14. La Porta, A., Slusher, R. E. & Yurke, B. Back-action evading measurements of an optical field using parametric down conversion. *Phys. Rev. Lett.* **62**, 28–31 (1989).
15. Riek, C. *et al.* Direct sampling of electric-field vacuum fluctuations. *Science* **350**, 420–423 (2015).
16. Moskalenko, A. S., Riek, C., Seletskiy, D. V., Burkard, G. & Leitenstorfer, A. Paraxial theory of direct electro-optic sampling of the quantum vacuum. *Phys. Rev. Lett.* **115**, 263601 (2015).
17. Esposito, M. *et al.* Photon number statistics uncover the fluctuations in non-equilibrium lattice dynamics. *Nat. Commun.* **6**, 10249 (2015).
18. Benea-Chelms, I.-C. *et al.* Subcycle measurement of intensity correlations in the terahertz frequency range. *Phys. Rev. A* **93**, 043812 (2016).
19. Glauber, R. J. Coherent and incoherent states of the radiation field. *Phys. Rev.* **131**, 2766–2788 (1963).
20. Huber, R., Brodschelm, A., Tauser, F. & Leitenstorfer, A. Generation and field-resolved detection of femtosecond electromagnetic pulses tunable up to 41 THz. *Appl. Phys. Lett.* **76**, 3191–3193 (2000).
21. Wasilewski, W., Lvovsky, A. I., Banaszek, K. & Radzewicz, C. Pulsed squeezed light: simultaneous squeezing of multiple modes. *Phys. Rev. A* **73**, 063819 (2006).
22. Shaked, Y., Pomerantz, R., Vered, R. Z. & Pe'er, A. Observing the nonclassical nature of ultra-broadband bi-photons at ultrafast speed. *New J. Phys.* **16**, 053012 (2014).
23. Hong, C. K., Ou, Z. Y. & Mandel, L. Measurement of subpicosecond time intervals between two photons by interference. *Phys. Rev. Lett.* **59**, 2044–2046 (1987).
24. Lu, E. Y. C. Quantum correlations in two-photon amplification. *Lett. Nuovo Cimento* **3**, 585–589 (1972).
25. Yablonovitch, E. Accelerating reference frame for electromagnetic waves in a rapidly growing plasma: Unruh–Davies–Fulling–DeWitt radiation and the nonadiabatic Casimir effect. *Phys. Rev. Lett.* **62**, 1742–1745 (1989).
26. Smithey, D. T., Beck, M., Raymer, M. G. & Faridani, A. Measurement of the Wigner distribution and the density matrix of a light mode using optical homodyne tomography: applications to squeezed states and the vacuum. *Phys. Rev. Lett.* **70**, 1244–1247 (1993).
27. Günter, G. *et al.* Sub-cycle switch-on of ultrastrong light–matter interaction. *Nature* **458**, 178–181 (2009).
28. Kira, M., Koch, S. W., Smith, R. P., Hunter, A. E. & Cundiff, S. T. Quantum spectroscopy with Schrödinger-cat states. *Nat. Phys.* **7**, 799–804 (2011).

Acknowledgements We thank W. Belzig and D. Brida for discussions. Support by ERC Advanced Grant 290876 ‘UltraPhase’, by DFG via SFB767 and by NSF via a Postdoc Fellowship for D.V.S. (award number 1160764) is acknowledged.

Author Contributions A.L. conceived the idea and wrote the first version of the paper. C.R., D.V.S. and A.L. designed the experiment. C.R., P.S., M.S. and D.V.S. performed the measurements and analysed the data. A.S.M. and G.B. worked out the theoretical description. All authors discussed the results and contributed to the writing of the final manuscript.

Author Information Reprints and permissions information is available at www.nature.com/reprints. The authors declare no competing financial interests. Readers are welcome to comment on the online version of the paper. Correspondence and requests for materials should be addressed to A.L. (aleitens@uni-konstanz.de).

Reviewer Information *Nature* thanks M. Bellini, J. Faist, D. Fausti and the other anonymous reviewer(s) for their contribution to the peer review of this work.

METHODS

Readout of coherent field amplitude and quantum noise in electro-optic sampling. Owing to the electro-optic (Pockels) effect, the electric field amplitude E_{MIR} of an electromagnetic wave propagating in a detector crystal (DX) with second-order nonlinearity leads to a quasi-instantaneous change in refractive index $\Delta n \propto E_{\text{MIR}}$. The induced birefringence causes a modified polarization state of a co-propagating probe pulse, which can be analysed using ellipsometry. In our geometry, we sample only one linear polarization component, which is perpendicular to the electric field of the NIR probe. The information about the temporal structure of E_{MIR} then results from repeated measurements sampling at different time delays t_D between the ultrashort probe and the electric field transient^{15,29}. The frequency bandwidth of this method is ultimately limited by the intensity envelope or 'pulse duration' of the probe, which needs to be close to or shorter than a half-cycle period of $E_{\text{MIR}}(t_D)$. The noise level of such measurements is determined by the shot noise due to the quantized flux of high-frequency probe photons¹⁶. We work with a repetition rate of our probe pulses of 40 MHz. Every second pulse is removed from the pump pulse train, resulting in a modulation frequency of 20 MHz where the coherent field amplitude $E_{\text{MIR}}(t_D)$ is decoded by lock-in detection. A detailed sketch of the experimental set-up is provided in Extended Data Fig. 1.

For the quantum noise measurements, the probe can be considered as being divided into two sub-pulse trains, with one sampling the potentially non-classical state coming from a synchronized emitter and the other measuring the bare vacuum noise as a reference. In our set-up, we detect both signals simultaneously by taking lock-in measurements in two orthogonal channels locked to a 10-MHz reference input derived from the 20-MHz pump by frequency division (see Extended Data Fig. 2). We then compute the r.m.s. noise levels of both sub-readouts and subtract them. The relative differential noise (RDN) that is recorded corresponds to the following physical quantity:

$$\begin{aligned} \text{RDN}(t_D) &= \frac{\sqrt{\Delta E_{\text{SN}}^2 + \Delta E_{\text{rms}}^2(t_D)} - \sqrt{\Delta E_{\text{SN}}^2 + \Delta E_{\text{vac}}^2}}{\sqrt{\Delta E_{\text{SN}}^2 + \Delta E_{\text{vac}}^2}} \\ &\approx [\Delta E_{\text{rms}}(t_D) - \Delta E_{\text{vac}}] \frac{\Delta E_{\text{vac}}}{\Delta E_{\text{SN}}} \end{aligned} \quad (4)$$

Here, $\Delta E_{\text{rms}}(t_D)$ is the standard deviation of the electric field sampled at a delay time t_D , ΔE_{vac} is the fluctuation amplitude of bare vacuum and ΔE_{SN} is the shot-noise equivalent field^{15,16} of the electro-optic detection. We compute $\Delta E_{\text{vac}} = 24 \pm 4 \text{ V cm}^{-1}$ and $\Delta E_{\text{SN}} = 81 \pm 16 \text{ V cm}^{-1}$ on the basis of the methods presented in ref. 15 and the slightly modified detection parameters of our set-up. Statistical summation of both values and normalization to the bare shot noise results in a 4% contribution of bare MIR vacuum noise to the fluctuations measured with the electro-optic detection in our configuration when no squeezed field is present. The linearized approximation in the right-most expression in equation (4) is used in Fig. 1c. It holds in the limit of moderate deviations of $\Delta E_{\text{rms}}(t_D)$ from ΔE_{vac} . The analysis in Fig. 4 is carried out taking into account the precise relationship between RDN and $\Delta E_{\text{rms}}(t_D)$ from the centre expression of equation (4). In contrast to the absolute measurement of the vacuum fluctuation amplitude¹⁵, we can now perform a relative measurement, which is superior in terms of robustness against any pickup noise and drift. Note that the detection bandwidth does not enter into the final result of this relative measurement. The precise setting of the radio-frequency lock-in influences only the signal-to-noise ratio of the RDN readout and has to be optimized with respect to the specific dwell times in an individual scan over t_D . See Extended Data Fig. 3 for a radio-frequency spectrum illustrating the white readout noise and electronic background of the detector. The possibility that the RDN patterns detected here might arise owing to a dependence of the electronic readout noise of the detector on the coherent amplitude or to technical noise of the transients is excluded by the measurements and arguments related to Extended Data Fig. 4.

Highly synchronous pump and probe pulse trains with minimum amplitude fluctuations are provided by a compact femtosecond Er:fibre laser system³⁰ that is based entirely on telecom components. By working at the highest possible lock-in frequencies for both the coherent field and RDN readouts, we ensure minimum timing jitter of 1 attosecond between pump and probe³¹, and quantum-limited amplitude fluctuations. Ultimately, these facts allow us to operate in a regime in which any technical noise of the set-up is negligible.

Collimation of the total field from the generation crystal (GX) is carried out with a gold-coated off-axis parabolic mirror of focal length $f = 15 \text{ mm}$ and numerical aperture $\text{NA} = 0.5$; the probe pulse is coupled in under s-polarized reflection on a polished Si wafer with a thickness of $500 \mu\text{m}$ that is inserted under Brewster's angle for the MIR; and another off-axis paraboloid ($f = 15 \text{ mm}$, $\text{NA} = 0.5$) serves to focus both signal and probe into the DX.

Theoretical considerations leading to equations (1) and (2). The generation of the quantum electric field patterns in our experiment can be understood as a series of two subsequent nonlinear processes of second order. First, a few-femtosecond pump pulse in the NIR produces an ultrashort and coherent electric field transient $E_{\text{MIR}}(t)$ at MIR frequencies Ω by optical rectification in a GX. This step corresponds to a difference-frequency mixing process within the broadband spectrum of the pump, resulting in an identical carrier-envelope phase for MIR transients in the entire pulse train produced by the mode-locked laser system²⁰.

In the second step, $E_{\text{MIR}}(t)$ starts driving the second-order nonlinearity in the GX. We adopt propagation of plane waves in the nonlinear element along the z axis from $-l/2$ to $l/2$ and an appropriate mutual orientation of pump field polarization and GX. The one-dimensional picture is well justified in our geometry because the thicknesses of both the GX and DX are smaller than the Rayleigh range of the MIR radiation that is generated. Together with the high-NA off-axis parabolic mirrors, this fact ensures proper matching to a single transverse mode. The nonlinear coefficient d is proportional to the second-order nonlinearity $\chi^{(2)}$ of the emitter material³²; n is the linear refractive index. All susceptibilities may be assumed to be dispersionless when the MIR frequencies Ω are far from the electronic and optical phonon resonances of the medium. In the vacuum picture³³, the total MIR quantum field can be written $\hat{E}_{\text{MIR}} = E_{\text{MIR}} + \delta\hat{E}_{\text{MIR}}$, with the coherent amplitude $E_{\text{MIR}} = \langle \hat{E}_{\text{MIR}} \rangle$ and a pure quantum correction $\delta\hat{E}_{\text{MIR}}$. Locally, \hat{E}_{MIR} induces the second-order nonlinear polarization $\hat{P}^{(2)} = -\epsilon_0 d \hat{E}_{\text{MIR}} \hat{E}_{\text{MIR}}$, which acts as a source in the wave equation. We restrict ourselves to small pump depletion by omitting the correction to the coherent part and neglect the second-order terms in $\delta\hat{E}_{\text{MIR}}$. The slowly varying amplitude approximation³² then leads to

$$\frac{\partial [\delta\hat{E}_{\text{MIR}}(z, \Omega)]}{\partial z} = -i \frac{\Omega d}{nc} \int_{-\infty}^{\infty} E_{\text{MIR}}^*(z, \Omega' - \Omega) \delta\hat{E}_{\text{MIR}}(z, \Omega') d\Omega'$$

Transforming back into the time domain and using a retarded reference frame with $t' = t - zn/c$, $z' = z$, $\delta\hat{E}_{\text{MIR}}(z', t') = \delta\hat{E}_{\text{MIR}}(z, t)$ and $E_{\text{MIR}}'(z', t') = E_{\text{MIR}}(z, t)$, we obtain

$$\frac{\partial [\delta\hat{E}_{\text{MIR}}'(z', t')]}{\partial z'} = \frac{d}{nc} \left\{ \frac{\partial [E_{\text{MIR}}'(z', t')]}{\partial t'} \delta\hat{E}_{\text{MIR}}'(z', t') + E_{\text{MIR}}'(z', t') \frac{\partial [\delta\hat{E}_{\text{MIR}}'(z', t')]}{\partial t'} \right\} \quad (5)$$

As long as deviations of the quantum field from the level of bare vacuum remain moderate, the temporal derivative of $\delta\hat{E}_{\text{MIR}}'(z', t')$ is negligible and we can omit the second term in the braces on the right-hand side of equation (5). The same term vanishes even for large squeezing when $E_{\text{MIR}}'(z', t')$ is sufficiently small. In both cases, an analytical solution of the partial differential equation is straightforward by integrating over z' . Returning to the original reference frame, the field at the exit surface of the GX, $\delta\hat{E}_{\text{MIR},\text{out}}(t) \equiv \delta\hat{E}_{\text{MIR}}(z = l/2, t)$, can be expressed as

$$\delta\hat{E}_{\text{MIR},\text{out}}(t) = e^{f(t)} \delta\hat{E}_{\text{MIR},\text{in}}\left(t - \frac{nl}{c}\right)$$

where $\delta\hat{E}_{\text{MIR},\text{in}}(t) \equiv \delta\hat{E}_{\text{MIR}}(z = -l/2, t)$ and

$$f(t) = \frac{dl}{nc} \frac{\partial [E_{\text{MIR}}(z = l/2, t)]}{\partial t}$$

recovers equation (2). Then, calculating the r.m.s. standard deviation $\Delta E_{\text{rms}}(t) \equiv \langle \delta\hat{E}_{\text{MIR},\text{out}}^2 \rangle^{1/2}(t)$ at the end of the nonlinear section results in

$$\Delta E_{\text{rms}}(t) = e^{f(t)} \sqrt{\langle \delta\hat{E}_{\text{MIR},\text{in}}^2 \left(t - \frac{nl}{c}\right) \rangle}$$

Equation (1) follows from a bare vacuum or fully coherent input, as in our experiment. In this case, $\langle \delta\hat{E}_{\text{MIR},\text{in}}^2 \rangle^{1/2}(t)$ is given by the r.m.s. vacuum electric field ΔE_{vac} .

Time-domain noise patterns and temporal changes of the local phase velocity. The Pockels effect³² causes a change in refractive index $\Delta n = rn^3 E_{\text{MIR}}$, with the effective electro-optic coefficient $r = -d/n^4$ linking $\partial E_{\text{MIR}}/\partial t$ and therefore $f(t)$ to accelerations and retardations of the local reference frame. The linear refractive index is defined as the ratio between the velocity of light in vacuum c and the local phase velocity v_{loc} : $n(t) = c/v_{\text{loc}}(t)$. Together with equation (2), we find

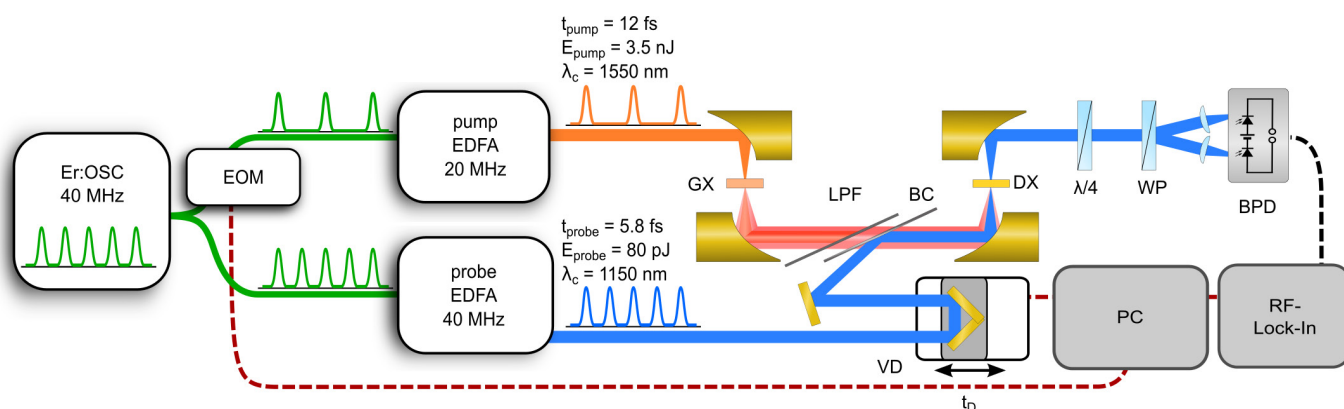
$$f(t) = -\frac{l}{c} \frac{\partial n}{\partial t} = l \frac{n^2}{c^2} \frac{\partial v_{\text{loc}}}{\partial t} \quad (6)$$

to first order in Δn . This expression is of general character because it does not depend on the specific nonlinearity used to induce the phase shifts that result in squeezing of the electromagnetic field and ultimately the emission of non-classical radiation. For example, analogous noise patterns to those found in our experiments might result from direct modulation of v_{loc} by the NIR pump intensity $I_p(t)$ via

third-order effects causing a nonlinear index of refraction n_2 and therefore $\Delta n(t) = n_2 I_p(t)$. It is clear from equations (1), (2) and (6) that excess noise with respect to the bare vacuum level is linked to acceleration of the local reference frame, that is, $\partial v_{loc}/\partial t > 0$. On the other hand, retardation with $\partial v_{loc}/\partial t < 0$ underlies a decrease in the local quantum fluctuations. These facts lead us to suggest a generalized understanding of quadratures in a time-domain context, as outlined in the conclusion of the main text.

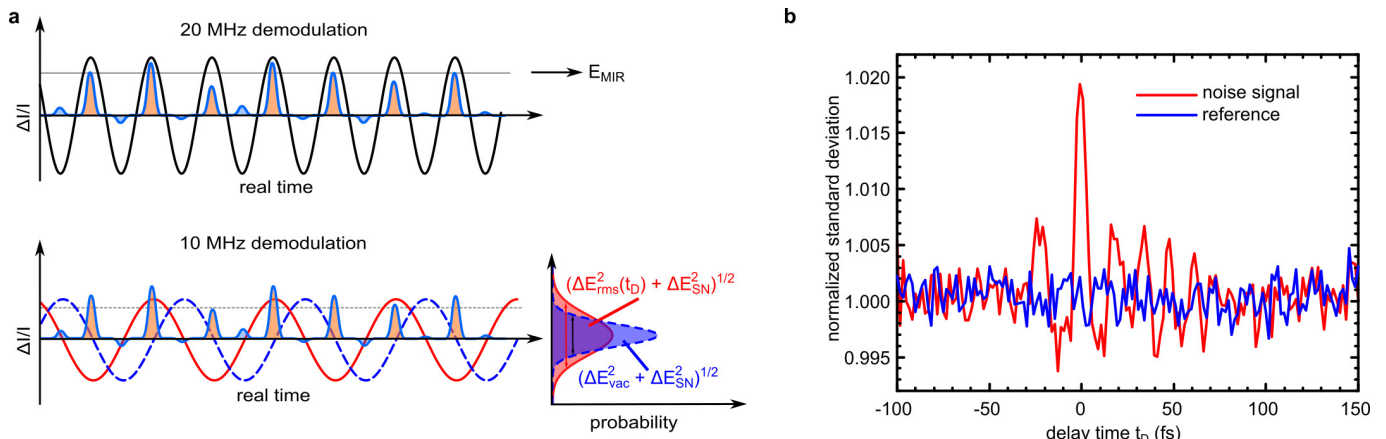
Data availability. The data that support the findings of this study are available from the corresponding author upon reasonable request.

29. Gallot, G. & Grischkowsky, D. Electro-optic detection of terahertz radiation. *J. Opt. Soc. Am. B* **16**, 1204–1212 (1999).
30. Brida, D., Krauss, G., Sell, A. & Leitenstorfer, A. Ultrabroadband Er: fiber lasers. *Laser Photonics Rev.* **8**, 409–428 (2014).
31. Adler, F., Sell, A., Sotier, F., Huber, R. & Leitenstorfer, A. Attosecond relative timing jitter and 13 fs tunable pulses from a two-branch Er: fiber laser. *Opt. Lett.* **32**, 3504–3506 (2007).
32. Boyd, R. W. *Nonlinear Optics* 3rd edn, Chs 9, 11 (Academic Press, 2008).
33. Knight, P. & Allen, L. *Concepts of Quantum Optics* 71–72 (Pergamon Press, 1983).



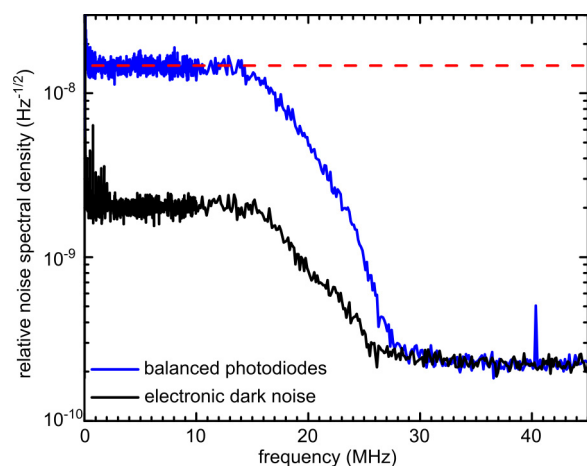
Extended Data Figure 1 | Sketch of the complete set-up underlying the experiments. A mode-locked Er:fibre laser oscillator (Er:OSC) forms a train of femtosecond pulses at a repetition rate of 40 MHz (green). After a fibre-optic beam splitter, an electro-optic modulator (EOM) removes every second pulse in the pump branch (top), reducing the repetition rate to 20 MHz, and 12-fs pulses of centre wavelength $\lambda_c = 1,550$ nm are generated by an Er:doped-fibre amplifier (pump EDFA) with subsequent pulse compression (orange pulse train). A pulse energy $E_{\text{pump}} = 3.5$ nJ is applied to pump the GaSe generation crystal (GX). The pulse train seeding the probe amplifier (probe EDFA) is left at a rate of 40 MHz and compressed to a duration of 5.8 fs and centre wavelength $\lambda_c = 1,150$ nm (blue pulse train). Eventually, a pulse energy of 120 pJ from this branch is available for probing the electro-optic effect in the AgGaS₂ detector crystal (DX). Details on the laser technology are found in ref. 30. The NIR pump beam is focused into the GX by an off-axis parabolic mirror (sketched in yellow). A MIR electric field transient (red beam path) is generated by the second-order nonlinearity of the GX, collimated by another parabolic mirror and sent through a thin GaSb wafer acting as low-pass filter (LPF).

This component is inserted at Brewster's angle for minimum loss of the MIR field and complete suppression of the NIR pump. The probe pulse train travels over a variable optical delay stage (VD) to set the relative timing t_D between pump and probe. It is reflected as s-polarized at a silicon beam combiner (BC), which is also inserted at Brewster's angle with respect to the p-polarized MIR field. Both beams are focused to co-propagate inside the DX. The probe pulse train is then collimated by a final off-axis parabola and sent through an ellipsometer that consists of an achromatic quarter-wave plate ($\lambda/4$) and a Wollaston prism (WP). A balanced pair of photodiodes (BPD) detects a differential photocurrent, which is proportional to the MIR electric field amplitude that has been co-propagating with the probe. In total, only $E_{\text{probe}} = 80$ pJ of probe pulse energy arrives at the BPD, owing to optical losses. Signals are demodulated at the Nyquist frequency of 20 MHz by a radio-frequency lock-in amplifier (RF lock-in) referenced to the EOM that picks every second pulse out of the pump pulse train. Signal collection and control of the VD are carried out by a personal computer (PC). An in-depth evaluation of the electro-optic sampling scheme is found in ref. 29.

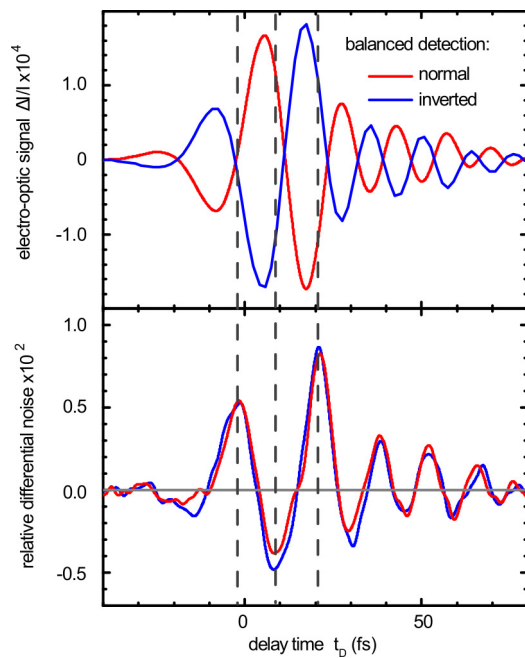


Extended Data Figure 2 | Explaining the concept of differential quantum sampling. **a**, Lock-in demodulation scheme for obtaining coherent amplitude and RDN. Individual readout values for the differential photocurrent $\Delta I/I$ are sketched as a function of real time. The readouts carrying signal due to pumping of the GX are red and the sub-pulse train sampling bare vacuum input is shown in blue. The time interval of 25 ns between each probe pulse is given by the inverse of the probe repetition rate of 40 MHz. Demodulation of the coherent field amplitude E_{MIR} is visualized in the top panel: the phase of the lock-in measurement at a reference frequency of 20 MHz is set such that the maximum difference between the average amplitude in the signal pulse train (red shading) and the reference pulse train (blue shading) is detected. Operating at the Nyquist frequency of the probe pulse train offers optimal performance in terms of amplitude and timing stability. Measurement of the RDN is illustrated in the bottom panel: we exploit two orthogonal readout phases at a reference frequency of 10 MHz to determine the level of fluctuations in the signal (red) and reference (blue) channels. In both cases, the standard deviation is computed; it corresponds to a convolution of the identical shot noise ΔE_{SN} in each channel and the noise due to the quantum fluctuations of the MIR electric field, which includes the pump-induced modulation of the quantum noise ΔE_{rms} in the signal channel and the bare vacuum noise ΔE_{vac} in the reference channel. The sketch on the right-hand side corresponds to a delay time with strong anti-squeezing: here the r.m.s. width of the noise distribution in the signal channel (red) is larger than that of the reference noise (blue). This case would result in

a positive value for the RDN. **b**, Individual readouts from the signal and reference channels. Raw data of a single scan over delay time t_D from the two separate noise channels of the differential detection scheme, collected within 150 s. The blue curve results from the reference channel, which has a radio-frequency phase set such that only the standard deviation of electro-optic readouts $\Delta I/I$ with no pump pulse present in the generation crystal is probed at a reference frequency of 10 MHz (blue sub-pulse train and dashed line in **a**). Detecting only the bare vacuum input, this channel shows no dependence on the relative time delay t_D between pumping and probing. In contrast, the channel with radio-frequency phase adjusted to sample the relative noise in the sub-pulse train that contains signals from the emitter excited by a pump pulse is plotted in red (noise signal, phase offset of 90° with respect to the reference channel; see red pulse train and line in **a**). Positions showing strong overshoot noise with respect to the vacuum reference are evident and indicate ‘anti-squeezing’, as sketched in an exaggerated way on the right-hand side of the bottom panel in **a**. But also delay times with the noise level of the red signal channel falling substantially below the blue reference data are clearly discernible, corresponding to ‘squeezing’ of the electric field with respect to the bare quantum vacuum. The data depicted in Figs 2 and 3 were processed in real time in the differential way described by equation (4) to obtain the RDN, subtracting any small variations that occur in the absolute noise floor of the laser or electro-optic detector. Statistics may be enhanced by averaging over multiple such scans.



Extended Data Figure 3 | Radio-frequency noise spectrum of the electro-optic detector. The relative noise spectral density at the output of the differential photodetector BPD, that is, at the input of the radio-frequency lock-in amplifier (see Extended Data Fig. 1), is shown. The black curve was recorded with the probe beam blocked and represents the electronic background (dark) noise of the system. The blue curve shows the noise spectrum under full illumination of the balanced photodiodes by the probe pulse train of repetition rate 40 MHz, but in the absence of any electro-optic signal input. The electronic low-pass filter is designed for a broad plateau of constant amplification and flat phase around the centre frequency of 10 MHz used for detection of the RDN (see Extended Data Fig. 2). The roll-off at a frequency of 20 MHz still leaves sufficient sensitivity for low-noise collection of the mean signal amplitudes, but results in a change in the radio-frequency phase angle with respect to the noise detection at 10 MHz, which needs to be adjusted correctly. The optical phase angle between the measured coherent field transients and the RDN patterns is not affected by this dispersion, because it results exclusively from scanning of the optical delay time t_D . The red dashed line represents the relative shot-noise level calculated for a Poisson input of 5×10^8 photoelectrons generated per probe pulse. It demonstrates that the broad noise plateau around 10 MHz is dominated by the shot noise of the probe photon flux, ensuring independence of the RDN signal from the measurement bandwidth set by the lock-in amplifier. Strong suppression of the 40 MHz signal from the fundamental pulse train is evident from the small maximum in the blue curve and helps to ensure adequate linearity of the electronic system.



Extended Data Figure 4 | Excluding nonlinearities in the readout electronics and technical noise of the coherent transients as potential spurious sources of RDN signals. A universal check for any influence in the noise readout due to the presence of finite coherent field amplitudes is as follows. We exchange the roles of the two photodiodes at the input of the differential detector by rotating the Wollaston prism (WP) in the ellipsometer by an angle of 180° (see Extended Data Fig. 1). In this way, the polarity of the classical electric transients is inverted electronically but not physically (in contrast to Fig. 2, in which the pump polarization on the generation crystal has been rotated by 90°), resulting in the blue and red curves in the top panel. If the differential noise traces depicted in the bottom panel were artefacts due to some response of the electronic noise detection to either the amplitude or the slope of the mean readout, then we would expect those signals to also invert sign, but this is not the case. The high degree of agreement between the blue and red noise traces in the bottom panel, corresponding to the original and electronically inverted transients in the top panel, is a good indication of the linearity of our readout scheme. The result of this procedure implies that our noise traces must have an optical origin and that they do not result from any spurious processes in the readout electronics. The noise patterns in the bottom panel also cannot result from amplitude or phase noise of the coherent transients: in both cases, the periodicity of the noise would follow the second harmonic of the coherent transients and no negative signals with respect to bare vacuum noise would be expected.